
Chapter II

Experimental Method

2.1 INTRODUCTION

2.2 SYNTHESIS OF BIODEGRADABLE MATRICES

2.2.1 *Materials*

2.2.2 *Solvent Casting*

2.2.2.1 Synthesis of Chitosan-based Polymeric Matrixes

2.2.2.2 Synthesis of Chitosan-based Solid Polymer Electrolyte

2.2.2.3 Synthesis of Chitosan-based Polymer Nanocomposites

2.3 60 MEV C⁺⁵ AND 100 MEV Ni⁺⁷ IONS IRRADIATION

2.3.1 *Overview–15UD Pelletron Accelerator*

2.3.2 *SHIs Irradiation Procedure*

2.3.3 *Energy Loss and Range of C⁺⁵ and Ni⁺⁷ ions in Polymeric Matrices*

2.4 CHARACTERIZATIONS OF BIODEGRADABLE MATRICES

2.4.1 *X-Ray Diffraction (XRD)*

2.4.2 *Fourier Transform Infrared Spectroscopy (FTIR)*

2.4.3 *UV-visible Spectroscopy*

2.4.4 *AC Electrical Frequency Response*

2.4.5 *Surface Analysis*

2.4.5.1 Scanning Electron Microscopy (SEM)

2.4.5.2 Atomic Force Microscopy (AFM)

REFERENCES

Chapter II

Experimental Method

2.1 Introduction

The response of biodegradable matrices are highly affected by the synthesis methodology along with the grade of the materials used and environmental conditions. The grade of materials and loading of fillers are imperative aspects of procuring superior matrices having good reproducibility is of crucial requirement. It encourages proper characterizations that have been precisely performed to procure the experimental data. Based on theoretic and illustrative models and descriptions, various aspects of matrices were analyzed and explained. In this chapter, the brief description of the solvent casting technique, the material used for preparation of different chitosan-based matrices, SHIs irradiation experiment and SRIM calculations, and the elementary features of the characterization techniques performed to characterize the biodegradable matrices.

2.2 Synthesis of Biodegradable Matrices

2.2.1 Materials

Powdered chitosan ($M_w=50-190$ kDa, degree of deacetylation 75–85%, CAS No. 9012-76-4), acetic acid (ACS reagent, $\geq 99.7\%$, CAS No. 64-19-7) and silver nanoparticles (<100 nm) were purchased from Sigma-Aldrich. Powered PEO ($M_w=300$ kDa, CAS No. 25322-68-3) was acquired from Alfa Aesar. Silver nitrate (Analytical grade, 98% purity, CAS No. 7761-88-8) with a molecular weight of 169.87 g/mol provided by Suvidhinath Laboratories, India.

2.2.2 Solvent Casting

Solvent cast approach is being a versatile tool that enables in broad-spectrum of applications in several disciplines thanks to ease of processability, cost-effective, needs not as much of instrumentations, and time conserving methodology [1]. This approach involving solubilization of polymer in an appropriate solvent to acquire a homogeneous film-forming solution, sometimes involvement of an elevated temperature is expected. The solvent casting is a nascent and former aspect to obtain a free-standing pristine as well as electrolytes and NPs

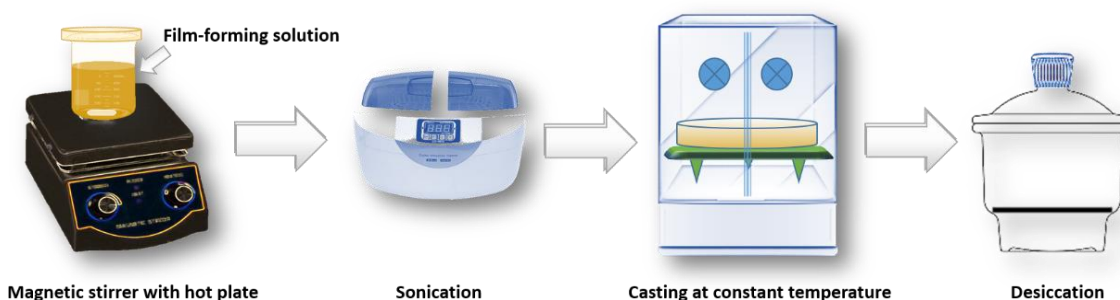


Figure 2.1 Schematic illustration for entire synthesis procedure

embedded matrices. Indeed, in the case of electrolytes, the required amount of salt can be directly dissolved within casting solution, while hybrid NPs matrix obtained by well-dispersed or sonicated NPs in the same or different solvent incorporate in casting solution. Acquired homogenous solution continued for 30 min of sonication (Citizen, Model CD 4820). A bath type sonicator having low ultrasonic power (90 W) with 42 kHz frequency is used at room temperature. Afterward, the film-forming solution was cast in a well-leveled petri dish or flatter surface. The phase and surface morphology of the matrix highly influence with evaporation rate of the solvent, which is controlled by solvent and solution concentration plus the pressure and temperature of the casting assembly [2]. The casted solution set aside to sit overnight to dry in the casting assembly with controlled temperature. Afterward, the film/matrix detached carefully and conditioned in desiccators up to further exploitation. This complete procedure is illustrated in [Figure 2.1](#).

2.2.2.1 Synthesis of Chitosan-based Polymeric Matrixes

Pristine chitosan matrix is prepared as the procedure described in section 2.2.2. To obtain a film-forming solution, an accurate amount of powered chitosan to attain the matrix with thickness of $\sim 80 \mu\text{m}$ vigorously stirred with 1% glacial acetic acid at ambient temperature, followed by sonication. To obtain the chitosan blend matrix with PEO of approximately the same thickness, equal weight percentage of powered polymers were individually diluted in 1% acetic acid solvent at room temperature. As the polymer completely dissolved, after filtration, both solutions were stirred together. Finally, the sonicated blend solution was poured into a well levelled and cleaned Teflon petri dish at room temperature. The desiccated film was detached and conditioned in desiccators.

2.2.2.2 Synthesis of Chitosan-based Solid Polymer Electrolyte

Similar to the pristine matrices, the chitosan-based SPE matrices were also synthesized using solvent casting. Dissolved chitosan suspension in 1.0% acetic acid solution was added separately with different amounts of silver nitrate at (60 ± 2) °C temperature. The polymer-salt complex was stirred persistently to get a homogeneous suspension. Each sonicated suspension was cast into a Teflon petri dish at room temperature to develop free-standing SPE matrices of ~ 60 μm thickness. For simplicity, concerning the wt% of silver ions, the detached SPE matrices with 0, 5, 10, 15, and 20 wt% of silver ions complex in chitosan acetate solution were labeled as CS, CSA, CSB, CSC, and CSD respectively. However, the consequence of recrystallization beyond 15% concentration, enables itself to constrict the discussions up to 15 wt%.

2.2.2.3 Synthesis of Chitosan-based Polymer Nanocomposites

Herewith, two hybrid matrices using Ag NPs were synthesized based on chitosan and CP blend matrices. The stock solutions of chitosan and CP blend to fabricate the chitosan-based silver nanoparticles (CSN) matrices and the chitosan-PEO blend based silver nanoparticles (CPN) matrices of mandatory thickness (~ 80 μm) were prepared by the solution casting approach. To synthesize the matrices with superior Ag NPs loading (>5 wt%), the powered Ag NPs directly dispersed into respective stock suspensions more willingly proposed than the chemical reduction route. Subsequently, the stock suspensions are well followed by sonication and casting tactics. At last, the CSN matrices separated and conveniently labeled as CSNA, CSNB, CSNC for 5, 10, and 15 wt% of Ag NPs doping concerning dry-based powered chitosan. Besides, the CPN matrices for equivalent doping were labeled as CPNA, CPNB, and CPNC respectively. Doping beyond a higher extent yielding highly heterogeneous matrices with unreliable Ag NPs distribution.

2.3 60 MeV C⁺⁵ and 100 MeV Ni⁺⁷ ions irradiation

2.3.1 Overview–15UD Pelletron Accelerator

In the present investigation of SHIs induced effects on biodegradable matrices, the energetic beam delivered from the 15UD Pelletron accelerator, a kind tandem Van de Graaff type

accelerator, accessible at IUAC New Delhi, India [3]. It is a versatile tool that can accelerate various ion as pulse and dc beam with energies ranging from few MeV to hundreds of MeV. Figure 15 and UD belong to "terminal voltage of 15 MV order" and "Unit Double" respectively. The entire assembly of the accelerator is organized vertically in an insulating tank comprising sulfur hexafluoride (SF_6) gas at 6-7 atmosphere pressure to obstruct discharging having 26.57 m of height and 5.5 m of diameter. A plan of the Pelletron Accelerator displaying the fundamental apparatuses illustrated in Figure 2.2 [4]. At above the vertex of the tank, there exist the versatile negative ion source, namely, Source of Negative Ions by Cesium Sputtering (SNICS), capable of generating a beam of negative ions starting each element that can form a stable negative ion. Utilizing the negative deck potential ($\sim 200\text{--}300\text{ keV}$) applied at the source enables the emitted negative ions toward the injector magnet analyzing the mass by deflecting

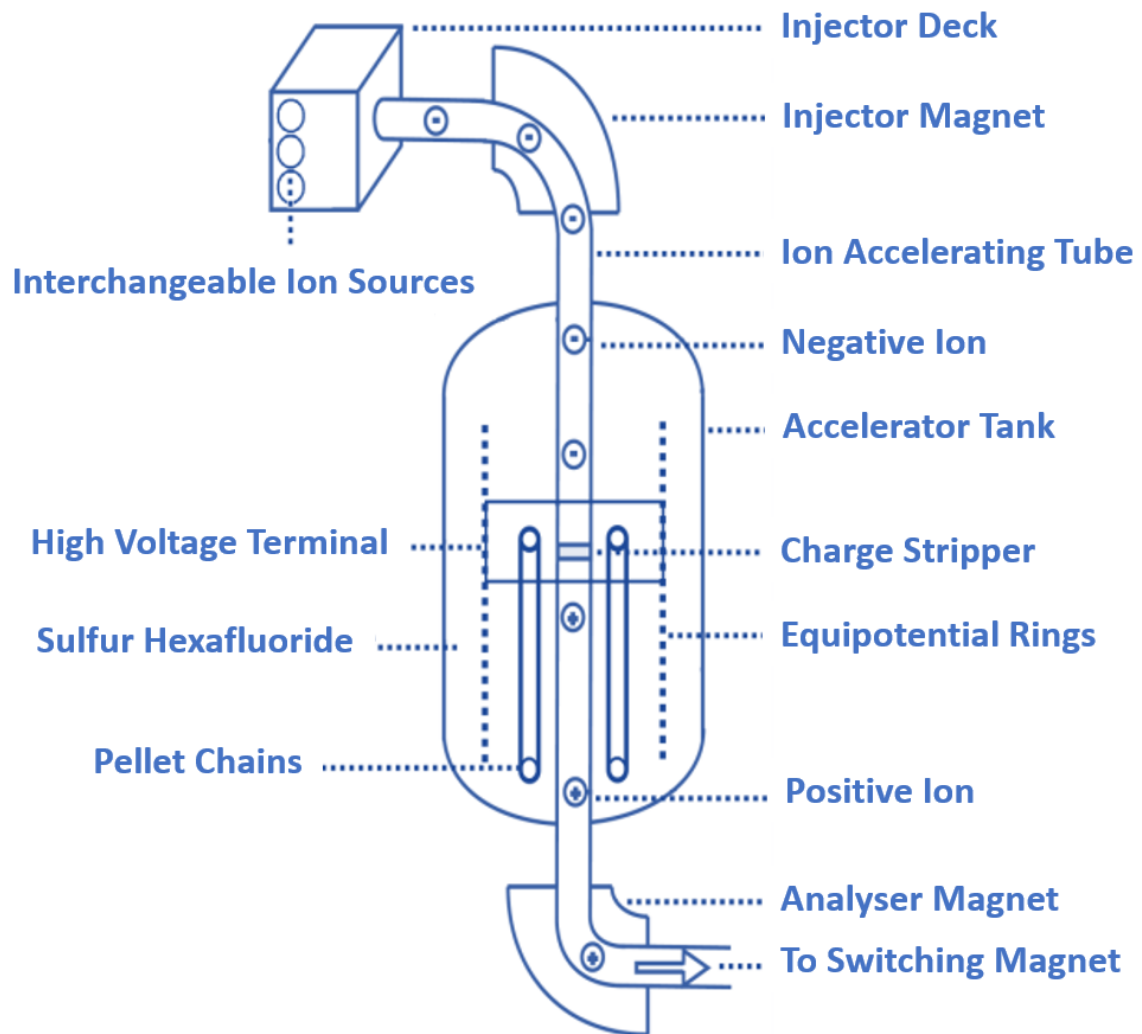


Figure 2.2 Schematic diagram of 15UD Pelletron Accelerator

the ions by 90° and injected the negative ions into the accelerating tube. A high voltage terminal is set up in the middle of the accelerating tank attained quite a higher potential of the order of 4 MV to 15 MV through charging with the help of the pellet chains. A terminal connected to an accelerating tube consisting of ceramic-titanium tubes maintaining potential gradient. The insulating column which supports the high potential terminal consists of 31 MV modules, 15 MV on either side of the terminal. The insulating column concerned in two sections, the higher section as low energy and the lower section as high energy concerning high terminal. In between, there exists no potential difference commonly referred Dead section, useful for equipment lodging. The charge stripper assembly made up of moderately thinner carbon foil or N_2 gas was equipped in the Dead section. As the accelerated negative ion passes through a stripper yielding positive ions. This positive ion influenced by high positive terminal potential and hence accelerated toward the ground potential applied at the bottom of the tank. Hence, the energy of accelerating ion at the bottom can be calculated using, $E = (q+1)V_T$ MeV, where q and V_T are referred to as ion charge state and terminal potential respectively. Finally, using the analyzer magnet, the obtained ion beam is directed to the particular section of the experimental high vacuum chamber as seen in Figure 2.3, where the irradiation of vacuum shielded desire target can be performed.

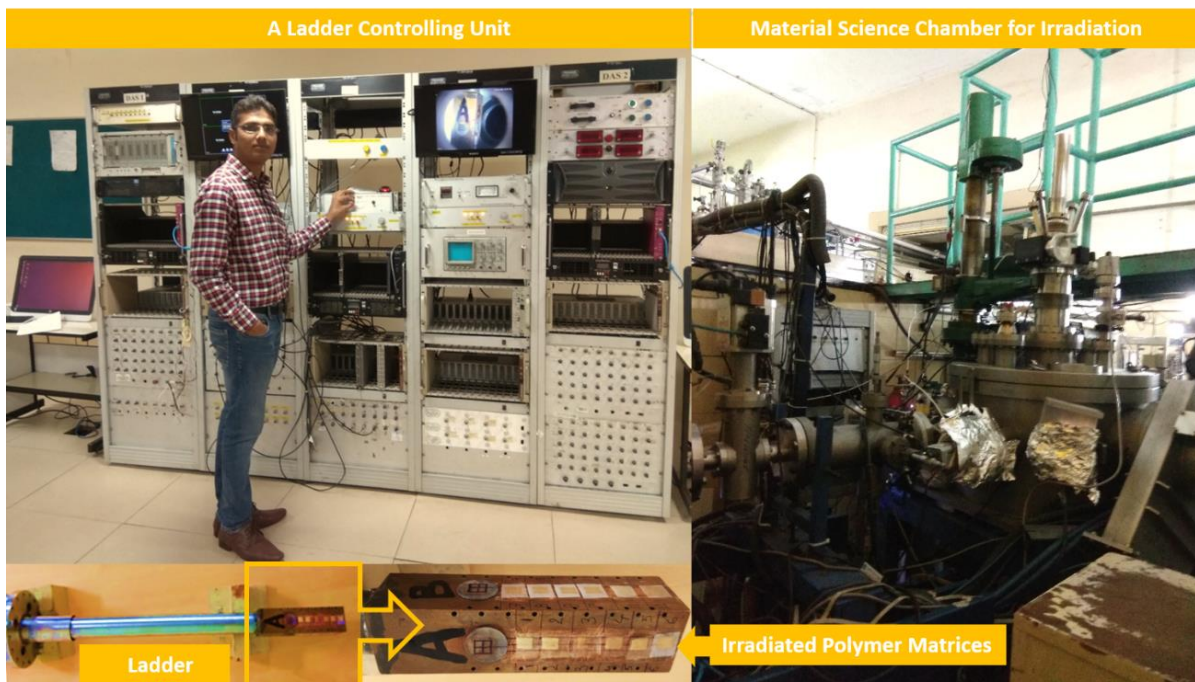


Figure 2.3 Actual images of a ladder controlling unit, ladder and Material Science high vacuum chamber

2.3.2 SHIs Irradiation Procedure

SHIs irradiation experiment performed using Material Science beamline upheld at 10^{-9} Torr pressure by directing the 60 MeV C^{+5} and 100 MeV Ni^{+7} ions beam in a separate shift. The ion beam focused on beam-viewing quartz at the top of the four-sided copper portion and then focused on pre-loaded $1.5 \times 1.5 \text{ cm}^2$ of the biodegradable polymeric matrices on the copper surface using two-way tape utilizing a ladder controlling unit, all these set up illustrated in Figure 2.3. The ongoing irradiation can be observed on-screen at the control unit with the help of a camera set up at an experimental high vacuum chamber upheld at 10^{-6} Torr. The $(1 \times 1) \text{ cm}^2$ section of pre-fixed matrices were sequentially scanned in the x–y coordinate by utilizing the electromagnetic scanner for homogeneous irradiation with low current ($\sim 0.5 \text{ pA}$) ion beam to prevent the heating effects. All the matrices were irradiated with the fluence of 1×10^{11} and $1 \times 10^{12} \text{ ions/cm}^2$ by utilizing respective ion beam. The irradiation time for the particular fluence is calculated using following formula.

$$Time = \frac{\text{ion fluence} \times \text{area of sample (cm}^2\text{)}}{\text{current (pA)} \times 6.25 \times 10^9}$$

2.3.3 Energy Loss and Range of C^{+5} and Ni^{+7} ions in Polymeric Matrices

Table 2.1 The simulated value of S_e , S_n , and R_p C^{+5} and Ni^{+7} ions in the respective matrix

Sample	C^{+5} (60 MeV)			Ni^{+7} (100 MeV)		
	S_e (keV/ μm)	S_n (keV/ μm)	R_p (μm)	S_e (keV/ μm)	S_n (keV/ μm)	R_p (μm)
CS	69.29	0.03889	554	1108	1.815	126
CP	95.25	0.05345	403	1524	2.494	92
CSC	99.81	0.05959	394	1534	2.691	93
CSN	108.7	0.06263	360	1686	2.979	84
CPN	112.9	0.06477	345	1762	3.070	80

As discussed in chapter 1, C^{+5} (60 MeV) and Ni^{+7} (100 MeV) losing their energies along its trajectory during the interaction within the polymeric materials through the electronic energy loss (S_e) and the nuclear energy loss (S_n). Simulating the SRIM 2013 code for the biodegradable matrices to estimate the S_e and S_n losses with their projected range (R_p) for C^{+5} and Ni^{+7} ions, and tabulated in Table 2.1.

2.4 Characterizations of Biodegradable Matrices

2.4.1 X-Ray Diffraction (XRD)

Necessity of XRD:

It is necessary to insight and explore the structural properties of the prepared materials. XRD analysis provides many facts and detailed information of crystal structures, phases and phase equilibriums, polycrystalline aggregation and crystal orientations as well as the relevant structural parameters, for instance, crystallinity, average particle/grain size, stress, strain, crystal defects, etc.

Fundamental principle:

In 1885, the German scientist Wilhelm Conrad Rontgen discovered X-ray, a kind of electromagnetic radiation with wavelength 0.01 to 100 Å. In crystal diffraction investigate, fundamentally the same diffraction phenomenon for electron and neutron can be used. The manner of the diffracted X-rays revealing the structural information of crystal. As the operated X-rays wavelength is of the order of the interatomic ordering in crystals. During the scientific discovery at Leeds, UK, in the summer of 1913, William Henry Bragg stated that “*It was a glorious time, when we worked far into every night with new worlds unfolding before us in the silent laboratory*” [5]. With a quick progress, father and his son William Lawrence Bragg explained the many inorganic crystals and diamond structures. W. L. Bragg uncovers its relevance to the structure determination of inorganic and organic materials, polymers, metals, alloys, compounds, minerals, etc. [6]. Depending on the atomic assembly either single crystal or chaotic like liquid or glassy, an explicit diffraction graphics, obeying the Bragg’s law $2d\sin\theta=n\lambda$, a special distribution and intensity obtained, which could explicitly determine the



Figure 2.4 Bruker D8-Advance diffractometer at IUAC, New Delhi

structural properties [7]. X-ray diffraction, a versatile technique, opened a link between atomic structure and the macroscopic world [8].

Authentic data collections and relevant structural analysis:

The XRD measurement of all biodegradable matrices was performed using a Bruker D8-Advance diffractometer at IUAC, New Delhi with a monochromatic wavelength of Cu- K_{α} radiation is 1.5418 Å as shown in Figure 2.4. Indeed, the polymeric matrices are assembly of longer macromolecular chains typically organized randomly. However, the chains may regularly organized in a small localized region at nanoscale yielding crystallite zones. From the change in peak broadening or FWHM of XRD patterns for semi-crystalline polymer can define the crystallite size [6]. The relation between average crystallite size (L) and peak broadening ($\beta_{1/2}$) could be explained by Scherrer equation, $L = 0.89\lambda/\beta_{1/2} \cos\theta$, where λ is X-ray wavelength [9].

2.4.2 Fourier Transform Infrared Spectroscopy (FTIR)

Necessity of FTIR:

The distinctive physical characteristics of a molecule can be studied via the vibration spectrum of the molecule, which exhibits the molecular structural feature. Indeed, the FTIR spectra is a

figure print of respective molecule, two distinct molecules never exhibits alike FTIR spectrum. Hence, this technique is an ingenious mode used for the characterization of polymeric matrices. It is capable to avail the important aspect such as macromolecular structural, vital groups, side chains, various linkages, kind of orientation, and vibrational modes can be inferred by the spectra analysis. Also, modifications in macromolecules by some means, that is, interaction with organic or inorganic molecules, metal, salt, nanoparticles, blending, plasticization, degradation and crosslinking can also be detectable.

Fundamental principle:

The basic technique used in FTIR is a consequence of vibrations associated with the atoms of a molecule. The total energy of a molecule can be inferred as a sum of vibrational, rotational, and electronic at any given instant [10]. Particularly, the vibrational energy associate with a molecule belongs to the IR region, and hence vibrational frequencies of molecules can be estimated. The molecule is subjected to the polychromatic ray in the IR section stimulates the interaction with a molecule only if there is a net change in dipole moment owing to the rotational and vibrational motion of the molecule. When there is resonance between the IR frequency and molecular vibrational frequency, then the energy absorbed having a certain frequency. It should be worth noting that the molecule absorbs the IR only if there exists a net change in dipole moment during vibration motion and is referred to as an IR-active molecule [11]. Typical vibration mode fascinated by IR radiation are stretching and deformation/bending linked with an influence in bond length and bond angle respectively. Principally, the starching mode either symmetric—involving low energy cause simultaneous increase or decrease in bond lengths or asymmetric—involving superior energy causes contrary change in bond lengths. The scissoring and rocking modes are referred to as in-plane bending vibrations, whereas wagging and twisting vibrations are referred to as out of plane bending vibrations. Also, the absorption frequency (f in s^{-1}) or wavenumber ($1/\lambda$ in cm^{-1}) of the molecules can be understood using Hook's law—a simple harmonic oscillations [10] as follow:

$$f = \frac{1}{\lambda} = \frac{1}{2\pi c} \sqrt{\frac{k}{\mu}}$$

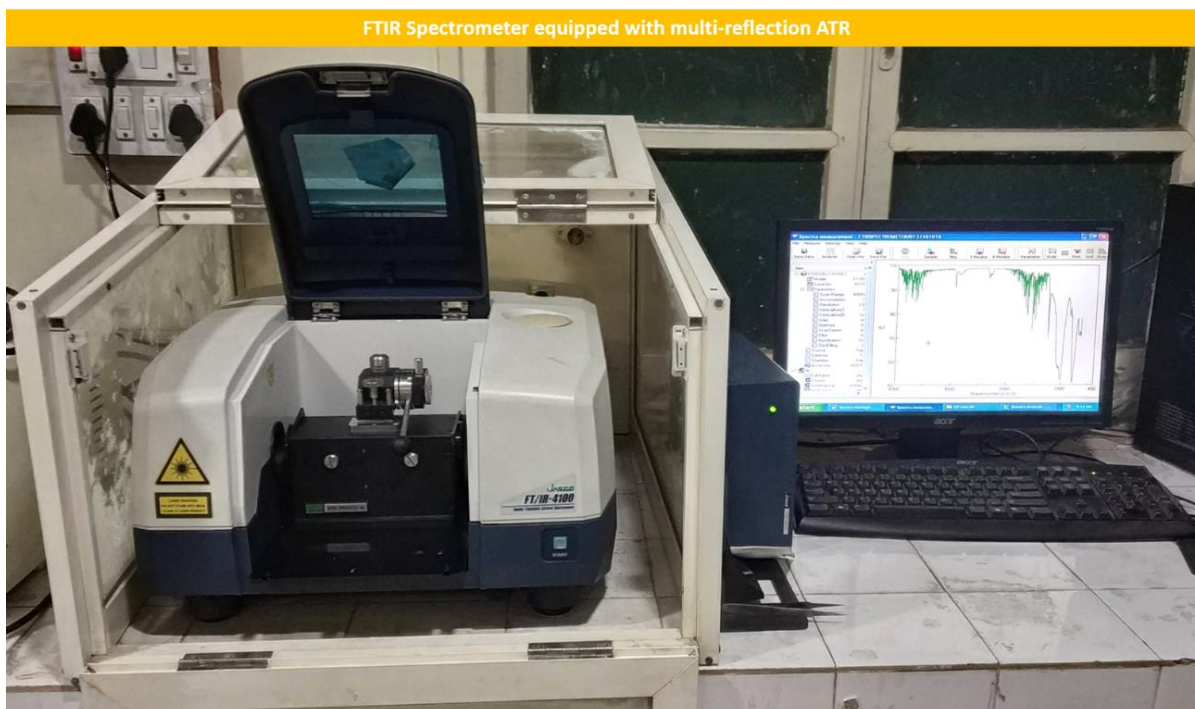


Figure 2.5 JASCO-4100 Spectrometer equipped with multi-reflection ATR PRO410-M at Department of Physics, Faculty of Science, MSU, Baroda

Where k is force constant (in dyne/cm) and μ is reduced mass (in g) to be considered as the strength of the chemical bond and reduced mass of the vibrating atoms. Hence, the vibrational modes shift toward higher wavenumber referred to as increased bond strength, while shift toward lower wave number ascribed to increased mass of atom [12].

Authentic data collections and relevant FTIR analysis:

As the matrix is subjected to polychromatic radiation in the mid IR range ($4000\text{--}400\text{ cm}^{-1}$) allowed to absorb the radiation of certain energy as per quantum theory formulates distinctive vibrational modes ascribing the type of bond in the macromolecule. To suppress the vibration mode of water vapor and air, a background should be recorded. The background spectra possess the entirely instrumental condition, and hence afterward the FTIR run for the actual matrix gives precise vibrational mode only belong to the sample. The excellence of peak measured from signal-to-noise ratio—directly related to the square root of scan time [13]. The FTIR spectra were recorded by comprising a spectrum after 100 successive scans in 120 seconds to ensure avoid the noise with 1 cm^{-1} resolution using a JASCO-4100 spectrometer in our laboratory at the Department of Physics, Faculty of Science, The M. S. University of Baroda, as observed from Figure 2.5. The spectra attained in Attenuated Total Reflectance (ATR) and

transmittance modes. ZnSe was used as an ATR crystal for which the incidence angle of the infrared radiation was 45° . The multi-reflection ATR (ATR PRO410-M) equipped with a spectrometer is an ingenious mode for polymeric matrices owing to an advantage of reproducibility, fast, precise and comparable due to elimination of the thickness effect.

2.4.3 UV-visible Spectroscopy

Necessity of UV-visible:

The UV-visible spectroscopy is comprehensively endorsed in characterization and investigation of polymeric material in the form of pristine, nanocomposites, blend, etc. can be processed in solid and liquid form with opaque, clear and colored materials. As a consequence of various parameters, a kind of electronic excitations transition, optical band gap (E_g), sign of chromophore, unsaturation, sp^3 hybridization, and surface plasmon resonance (SPR) of metallic NPs can be explored.

Fundamental principle:

As per quantum physics, the excitation of the electron is fascinated by reorganizing the valance electron of atoms or molecules through the absorption of certain energy in form of quanta. As a result, there is a transition of electrons to higher energy levels from the lower one. Eventually, the excited atoms or molecules relax themselves by re-emitting photons of energy equivalent

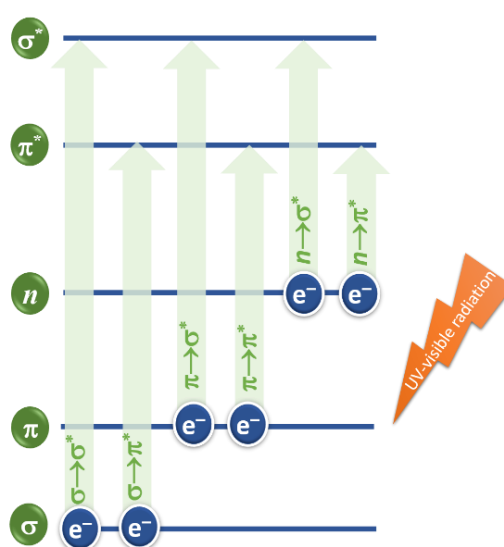


Figure 2.6 A schematic diagram of allowed electronic transitions due to absorption of UV-visible radiations

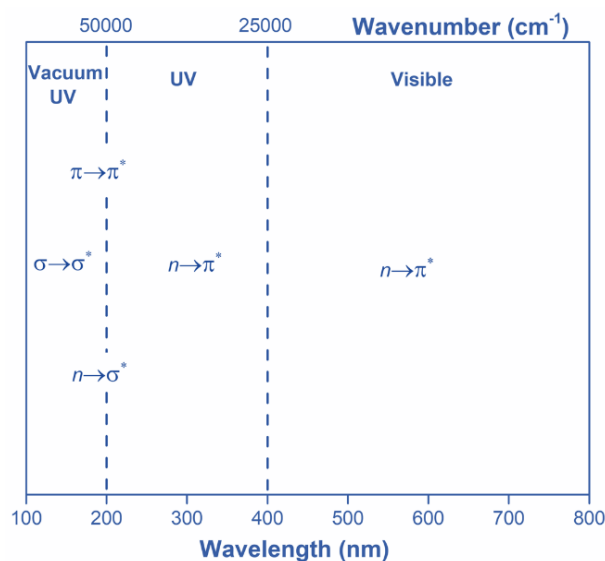


Figure 2.7 The wavelength region corresponds to molecular transitions due to interaction of UV-visible radiation with matter

©Wiley-VCH Verlag GmbH & Co. KGaA, 2015, doi:10.1002/9783527645602.ch24

to respective transitions that are simultaneously detected as a function of wavelength yielding the UV-visible absorption spectra. Since the released energies correspond to electron transition are unique for each species enable to characterize and recognize the constituents of a material. Hence, UV-visible spectroscopy is often referred to as electronic spectroscopy. The overlapped atomic orbits formed σ (bonding) and σ^* (antibonding) possessed single bond, π (bonding) and π^* (antibonding) indorsed double or triple bonds and nonbonding orbital (n) [14]. A schematic diagram of allowed electronic transitions due to the absorption of UV-visible radiations illustrated in Figure 2.6. Since the energy mandatory for $\sigma \rightarrow \sigma^*$ transition is exceeding the UV region. However, $n \rightarrow \sigma^*$, $n \rightarrow \pi^*$ and $\pi \rightarrow \pi^*$ transitions relatively required less energy lie in the UV-visible range [15]. The molecular transitions transpire on account of UV-visible radiation with matter as revealed from Figure 2.7. The $\pi \rightarrow \pi^*$ molecular transition attributed to the existence of chromophore having an unsaturated linkage, for instance, $C=O$, $C=C$, $C \equiv N$ etc. [14,15]. Also, charge transfer reaction and Interface design at the interface of polymer and inorganic fillers influence the molecular transitions [16].

Authentic data collections and relevant optical analysis:

The UV-visible spectra in the absorption mode of biodegradable matrices were acquired in a wavelength region of 200-800 nm using dual-beam Hitachi Model U-3300 spectrometer at IUAC, New Delhi as seen from Figure 2.8. Tauc's method was used to avail a kind of the



Figure 2.8 Hitachi Model U-3300 Spectrometer at IUAC, New Delhi

transition between the parabolic bands and to evaluate the optical energy bandgap (E_g) using the following equation [17]:

$$\alpha h\nu = B (h\nu - E_g)^n$$

where α is the absorption coefficient, $h\nu$ is the photon energy, n is the power that designates the transition processes in K-space, explicitly, direct or indirect and dipole mediated (allowed) or not (forbidden) ($n = 0.5, 1.5$ stand for a direct and indirect allowed, while 2 and 3 values correspond to direct and indirect forbidden transitions), $h\nu$ is the photon energy, E_g is the bandgap, and α is the absorption coefficient [17]. Using a satisfactory linear least-squares fit of $(\alpha h\nu)^{1/n} \rightarrow h\nu$ graphics with reliable goodness-of-fit (R^2) by extrapolating the $(\alpha h\nu)^{1/n}$ to the zero on $h\nu$ -axis yielding the value of E_g with standard deviation.

The carbonaceous compact cluster as inferred by Robertson and O'Reilly can be supposed as a system of autonomous cluster compose of the C_6 like structure [18]. Subsequently, Fink et al. revised the Robertson and O'Reilly model by considering the cluster structure as C_{60} instead of C_6 [19]. The number of carbon atoms per conjugation length (N) was evaluated by using the modified Fink model via the following relation [19]:

$$E_g = \frac{34.3}{\sqrt{N}} \text{ eV}$$

2.4.4 AC Electrical Frequency Response

Necessity of Dielectric spectroscopy:

The response of materials as an interaction with electromagnetic quantum mechanically allowed transitions between molecular energy state as inferred in FTIR and UV-visible spectroscopies involving rotational, vibrational, and electronic transitions having frequencies beyond 10^{12} Hz. Hence, the consequences of absorption and dielectric responses below these frequencies within materials can be insight by Broadband Dielectric Spectroscopy, which indorsed to the molecular dipole relaxation evolving from the reorientation movements of dipoles, the electrical conduction cascades ensuing from the motional drift of charge carriers (electrons, ions or charged defects) as well as the polarization at the interfaces owing to charge severance [20].

Fundamental principle:

Specifically, this technique is fairly suited to investigates the segmental dynamics of polymer *via* measuring the dipole moments of monomeric units because most polymers possess permanent molecular dipole moments [21]. The dielectric response of a polymeric system is mainly based on electrode/interfacial, orientation, atomic and electronic polarization of the component molecules. The electrode and interfacial polarisations attributed to the formation of double layers at matrix/electrode interface due to migration of charge carriers under the influence of external field and trapping of free as well as bound charge carriers mainly at interface in hybrid/heterogeneous system comprising with more than one phases respectively [22]. The orientational polarisation attributed to alignment of dipole moments appended to moieties and molecular functional groups dipole moments with varying external field [23]. The most polymeric dielectric responses involve the orientational polarisation along with segmental relaxation determined the macromolecular dynamics behavior at the nanoscale. The atomic and electronic polarizations attributed to dislocation of atomic nuclei relative to one another and shift or deformation of electron clouds of atom or molecules from nuclei for each atom [24]. The electrode and interfacial polarisations observed in frequencies below 10^3 and 10^6 Hz respectively and the orientational polarisations observed in intermediate frequencies window ($\sim 10^8$ to 10^{10} Hz) are characterized by relaxation frequency [20,23,25]. Whereas, the atomic and electronic polarizations characterized by resonance frequency observed in the IR region

($\sim 10^{11}$ to 10^{14} Hz) and UV-visible region ($\sim 10^{14}$ to 10^{17} Hz) [26]. The fundamental principle of frequency-domain dielectric spectroscopy is that the time-varying electric field is exploited across the electrode sorted with polymeric materials. The dipole associated with functional groups of macromolecules reoriented as per the frequency of applied field up to specific value of frequency indorsed to macromolecule natural frequency. The persuasive following nature of dipole to oscillating field does not perceive as the controlled frequencies transcends the natural frequency of dipole is inferred as dielectric relaxation. Consequently, the output current lagged behind with a certain phase shift with relative change in amplitude concerning the applied oscillating field/voltage yielding the fundamental dielectric response of materials [25]. As a result, the distinctive formalisms with their advantages and limitations implicated to analyze the obtained data in a complex plane appended with real and imaginary components.

Authentic data collections and relevant dielectric analysis:

The dielectric spectra of self-sustained pristine, blend, and hybrid matrices based on pristine and blend matrices were acquired by performing a precision Agilent E4980A LCR meter in 20 Hz to 2 MHz frequency window at physics department, school of science, Ahmedabad. Agilent 16451B solid dielectric test fixture used to affix the matrices between the electrodes at ambient temperature to procure the data *via* solely computer-assisted interface as displayed in Figure 2.9(a).

The dielectric data of SPE matrices were collected using a Solartron SI-1260 impedance gain/phase analyzer in our laboratory at the Department of Physics, Faculty of Science, The M.

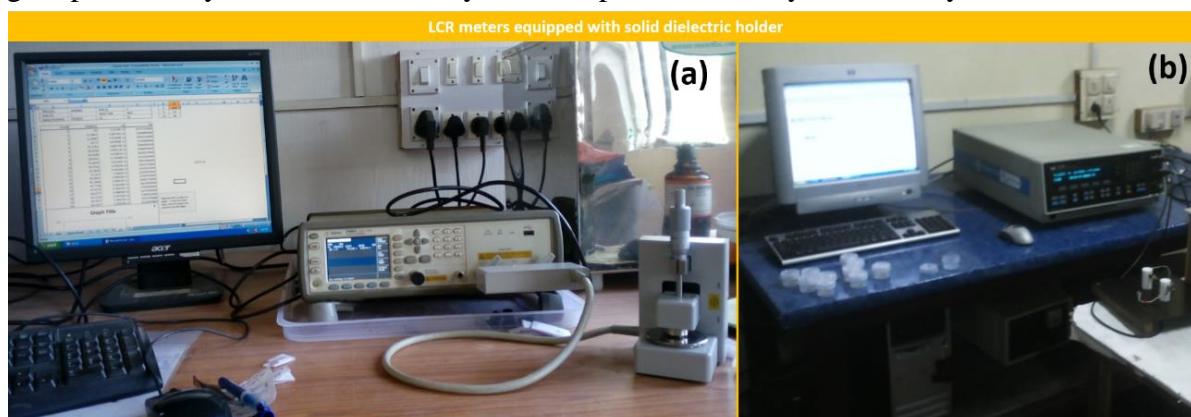


Figure 2.9 (a) Agilent E4980A LCR meter equipped with Agilent 16451B solid dielectric test fixture at physics department, school of science, Ahmedabad and (b) Solartron SI-1260 impedance gain/phase analyzer at Department of Physics, Faculty of Science, MSU, Baroda

S. University of Baroda, as illustrated in Figure 2.9(b). The self-standing matrices were sandwiched properly with adjustable spring tension between two silver electrodes. The impedance was measured in the frequency range of 10 Hz–10 MHz at ambient temperature with 1-V AC signal amplitude. The frequency-domain data were exported *via* a computer-aided programmed interface. The Z-View2 software was performed for comprehensive analysis of the distinctive dielectric formalism.

The real part (ϵ') and imaginary part (ϵ'') of complex permittivity (ϵ^*) calculated using the measured parallel capacitance (C_p) and parallel resistance (R_p) *via* the following equation:

$$\epsilon^*(f) = \left(\frac{C_p d}{\pi r^2 \epsilon_0} \right) - j \left(\frac{d}{\pi r^2 \omega R_p \epsilon_0} \right) = \epsilon'(f) - j\epsilon''(f)$$

where d is thickness of self-sustained matrix (in m), r is the radius of electrode–matrix contact area (in m), dielectric permittivity of air (ϵ_0) is $8.854 \times 10^{-12} \text{ C}^2/\text{Nm}^2$ and $j = \sqrt{-1}$.

The complex electric modulus (M^*) with real (M') and imaginary (M'') electric modulus can be obtained using the complex permittivity as expressed by the following equation [20]:

$$M^*(f) = \frac{1}{\epsilon^*(f)} = \frac{1}{\epsilon'(f) - j\epsilon''(f)} = M'(f) + jM''(f)$$

$$\text{where } M'(f) = \frac{\epsilon'(f)}{\epsilon'^2(f) + \epsilon''^2(f)} \text{ and } M''(f) = \frac{\epsilon''(f)}{\epsilon'^2(f) + \epsilon''^2(f)}$$

The Kohlrausch–Williams–Watt (KWW) model is a preferable adoption for the fitting of graphics by adjusting the variables ϕ_{KWW} and β_{KWW} to comprehend the molecular dynamics and conductivity relaxation [27].

$$M_{KWW}^*(\omega) = M_\infty \left[1 - \int_0^\infty e^{-i\omega t} \left(-\frac{d\phi_{KWW}}{dt} \right) dt \right]$$

$$\text{where } \phi_{KWW} = e^{(-t/\tau)\beta_{KWW}}$$

Particularly for an ideal Debye relaxation, the shape parameter β_{KWW} to be unity and exhibited a decreasing tendency with increasing deviation from ideal relaxation. The Kohlrausch–Williams–Watt (KWW) elicited empirical exponential function explicitly well-

fitted the experimental data of the frequency-dependent $M''(\omega)$ graphic in the frequency province was amended by Bergman and can be expressed as follows:

$$M''(\omega) = \frac{M''_{max}}{(1 - \beta_{KWW}) + \left[\left(\frac{\beta_{KWW}}{1 + \beta_{KWW}} \right) \left(\beta_{KWW} \left(\frac{f_{max}}{f} \right) + \left(\frac{f}{f_{max}} \right)^{\beta_{KWW}} \right) \right]}$$

where M''_{max} is the peak maxima of imaginary electric modulus and the corresponding frequency f_{max} at which peak maxima is estimated [28]. The reliable fitting enable using the figure of merit (FOM) estimation of experimental frequency-dependent $M''(\omega)$ values with simulated predictable values.

The complex conductivity (σ^*) can be expressed in terms of complex relative permittivity by the following equation [20].

$$\sigma^*(f) = j\varepsilon_0\omega\varepsilon^*(f) = \varepsilon_0\omega\varepsilon''(f) + j\varepsilon_0\omega\varepsilon'(f)$$

The real part of σ^* can be written as $\sigma(f) = \varepsilon_0\omega\varepsilon''(f)$. The total electrical conductivity, σ , appended to the plateau region figured at lower frequencies contributing as direct current, σ_{dc} , and the frequency-dependent dispersive region emerged at higher frequency contributing as alternate current, $\sigma_{ac}=B\omega^s$. The frequency-dependent conductivity principally obeys the Jonscher universal power model as follow [29]:

$$\sigma(f) = \sigma_{dc} + B\omega^s$$

The dimensionless fractional exponent “s” attained the values by assuring the condition $0 \leq s \leq 1$ and B is the pre-exponential parameter. The σ_{dc} is estimated by extrapolating the plateau graphics to zero frequency on σ -axis. As $\sigma_{ac}=B\omega^s$ can be equation rewritten as $\log(\sigma_{ac}) = \log(B) + s \log(\omega)$. Hence the slop ($d\sigma_{ac}/d\log\omega$) of $\log\sigma_{ac}$ vs $\log\omega$ graphic yielding the value of “s” by following the linear regression statistics at higher frequency window to suppress the circumstance of electrode and interfacial polarisations.

2.4.5 Surface Analysis

Surface structures exploitation of pristine, electrolyte, and hybrid biodegradable self-standing matrices were performed using Scanning Electron Microscopy and Atomic Force Microscopy.

2.4.5.1 Scanning Electron Microscopy (SEM)

Necessity of SEM:

The SEM is an incredibly expedient microscopic technique to collect the surface microstructural features. The change in morphological responses of surface under various conditions like SHIs irradiation, temperature, pressure, tensions, etching, synthesis methodologies can qualitative and quantitatively investigated in the studies of localized distribution and agglomeration of particles, composite characterizations, degradation, surface defect, porosity, grain size, crack propagation, miscibility of polymer blend etc. [4,11,30].

Fundamental principle:

In the microscopic technique, resolving power and contrast are vital aspects. The larger wavelength of about 380-760 nm of visible light constraining capability to resolve the image details of the light microscope is about 0.2 μm [31]. As per Louis de Broglie, the electrons possess a wavelike character and the wavelength of the electron is $\lambda_e = h/(2m_e eV)^{1/2}$ of the order of atomic-scale ~ 0.17 nm and can be tuned easily by changing the accelerating potential (V) to attain the superior resolution, that is, 1 nm or better [31]. Davisson and Germer revealed the scattering of electrons from a crystal as the X-rays do [32]. The fundamental need in SEM is to channelize the stable electron-beam mechanism similar to the light microscope, except with enhanced spatial resolution. However, the incident electron referred to as the primary electron enables to release of the secondary electron with sort of energies yielding focusing obstacle to



Figure 2.10 FESEM device of Zeiss, Merlin VP Compact at FCIPT, Gandhinagar

obtain the image. Hence an alternative mode of operation employed based on a scanning principle in which, the electron-beam by utilizing the electrostatic or magnetic fields confined finely having a small-diameter electron probe scanning the specimen [4]. The electrons probe spread laterally with a pear-shaped region of few microns referred as interaction volume upon penetration into the surface of a bulk specimen by gradually losing the energy by interacting with atoms [33]. As a result, a sort of signals, namely, secondary, backscattered electrons and characteristic X-rays that are collected by distinct detectors and promote processing yielding a micrograph or image with surface chemistry of specimen [34].

Authentic data collections and SEM image formation

The high-resolution SEM images of biodegradable matrices recorded using a FESEM device Merlin VP Compact, Zeiss displayed in Figure 2.10 with the magnification of 1000 to 50000 × with electron beam energy of 3 kV at FCIPT, Gandhinagar, Gujarat.

2.4.5.2 Atomic Force Microscopy (AFM)

Necessity of AFM:

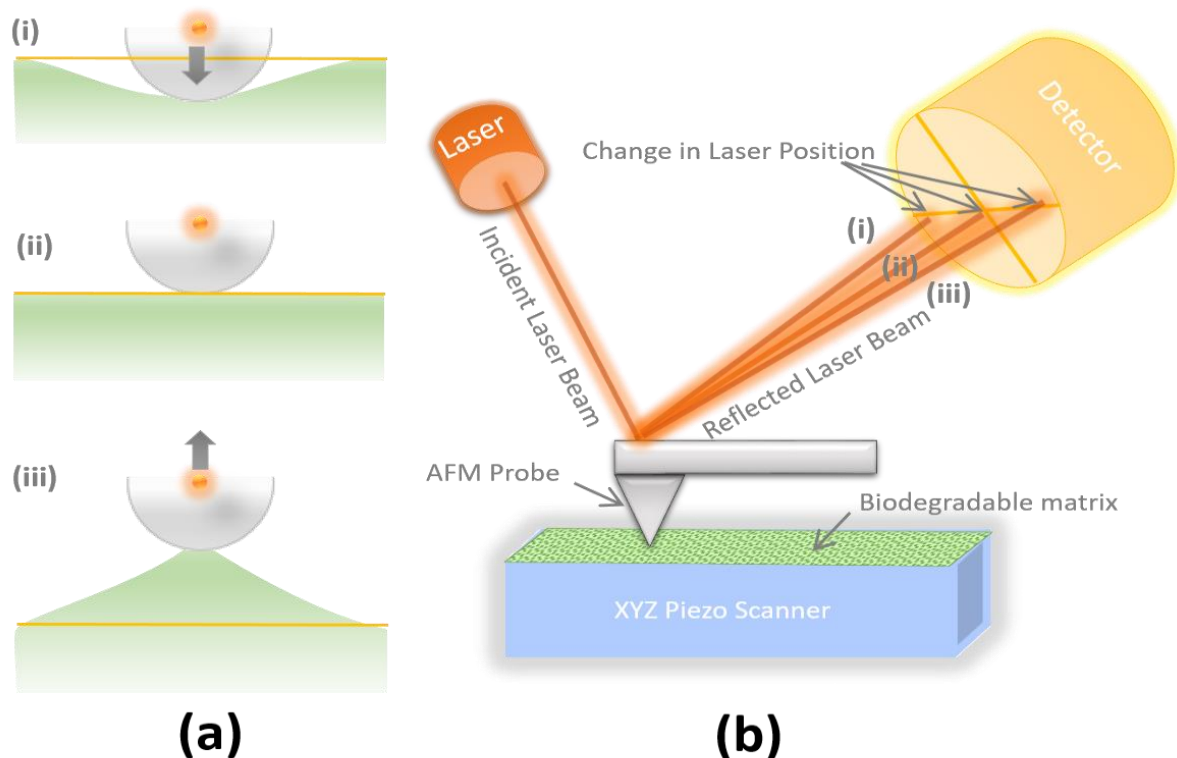


Figure 2.11 (a) Geometry between probe and surface (b) A schematic illustration of fundamental working principle of AFM

The AFM is to imperative approach in 3D surface imaging due to atomic-scale resolution of nm to Å extent equivalently processing synthetic to natural, solid to spongy, dry to wet as well as insulating to conducting materials. This technique adeptly avail the statistics involving qualitative and quantitative facts of specimen such as morphological texture, roughness, distribution and size of comprising particle or filler, phase separation, and many more as per requisites.

Fundamental principle:

The scanning of surface performed using a petite tip set with cantilever referred to as AFM probe experiences attractive and repulsive forces acted by surface atoms as per geometry between probe and surface texture as revealed in Figure 2.11(a). Consequently, the probe successively shifts in upward and downward directions and the corresponding shift in reflected laser beam measured using detector as depicted in Figure 2.11(b). The intensity and positional statistics of laser beam reflected from the top of the cantilever recorded by detector triggering respective signals enable to production of the AFM image [35]. In AFM technique according to various forces such as Van der Waals forces, mechanical contact force, electrostatic forces,



Figure 2.12 The AFM setups at IUAC, New Delhi

capillary forces, magnetic forces, chemical bonding, etc., distinctive AFM probe utilized in different disciplines as per needs.

Authentic data collections and AFM image formation

AFM has three key tactics of operation according to scanning procedure, explicitly, contact modes, non-contact mode, and tapping modes. In the present investigation, the scanning of all the biodegradable self-standing matrices have been performed in tapping mode. AFM Nanoscope Digital Instruments, Canberra, USA at IUAC, New Delhi was performed in air at ambient temperature as revealed from [Figure 2.12](#). This facility possess 0.5 N/m force constant and the AFM probe made of silicon nitride tip with 100 μm length of cantilever. Since SHIs induced topographical and morphological changes significantly affect the average surface roughness (R_a) were estimated, which enact an eminent and crucial role for polymeric materials in various disciplines for desired purposes [\[36–38\]](#).

REFERENCES

- [1] U. Siemann, Solvent cast technology – a versatile tool for thin film production, in: *Scatt. Methods Prop. Polym. Mater.*, Springer Berlin Heidelberg, Berlin, Heidelberg, 2005: pp. 1–14. doi:10.1007/b107336.
- [2] D.L. Chinaglia, R. Gregorio, J.C. Stefanello, R.A. Pisani Altafim, W. Wirges, F. Wang, R. Gerhard, Influence of the solvent evaporation rate on the crystalline phases of solution-cast poly(vinylidene fluoride) films, *J. Appl. Polym. Sci.* 116 (2009) n/a-n/a. doi:10.1002/app.31488.
- [3] www.iuac.res.in, (n.d.). <http://www.iuac.res.in/accel/pell/index.html>.
- [4] I.P. Jain, G. Agarwal, Ion beam induced surface and interface engineering, *Surf. Sci. Rep.* 66 (2011) 77–172. doi:10.1016/j.surfrep.2010.11.001.
- [5] A. Moscatelli, A new crystallography is born, *Nature*. 511 (2014) 7–7. doi:10.1038/nature13352.
- [6] C. Suryanarayana, M.G. Norton, *X-Ray Diffraction*, Springer US, Boston, MA, 1998. doi:10.1007/978-1-4899-0148-4.
- [7] P.W.H. Bragg, W.L. Bragg, The reflection of X-rays by crystals, *Proc. R. Soc. London. Ser. A, Contain. Pap. a Math. Phys. Character.* 88 (1913) 428–438. doi:10.1098/rspa.1913.0040.
- [8] D. Gevaux, The equation to bridge worlds, *Nature*. 511 (2014) 6–7. doi:10.1038/nature13351.
- [9] A.L. Patterson, The Scherrer Formula for X-Ray Particle Size Determination, *Phys. Rev.* 56 (1939) 978–982. doi:10.1103/PhysRev.56.978.
- [10] S. Wartewig, Basic Principles of Vibrational Spectroscopy, in: *IR Raman Spectrosc.*, Wiley-VCH Verlag GmbH & Co. KGaA, Weinheim, FRG, 2004: pp. 27–33. doi:10.1002/3527601635.ch4.
- [11] T.D. Schroeder, An undergraduate instrumental analysis course, 1975. doi:10.1021/ed052p229.
- [12] B. Karmakar, Fundamentals of Glass and Glass Nanocomposites, in: *Glas. Nanocomposites*, Elsevier, 2016: pp. 3–53. doi:10.1016/B978-0-323-39309-6.00001-8.
- [13] B.C. Smith, *Fundamentals of Fourier Transform Infrared Spectroscopy*, CRC Press, 2011. doi:10.1201/b10777.
- [14] M.H. Abou-Taleb, Characterization of Polymer Blends Using UV-Visible Spectroscopy, in: *Charact. Polym. Blends*, Wiley-VCH Verlag GmbH & Co. KGaA, Weinheim, Germany, 2014: pp. 789–820. doi:10.1002/9783527645602.ch24.
- [15] D.A. Long, *Undergraduate instrumental analysis* James W. Robinson, Eileen M. Skelly

- Frame and George M. Frame II. Marcel Dekker, New York, 6th edition, 2005, pp. xix + 1079. ISBN 0 824 75359 3, *J. Raman Spectrosc.* 36 (2005) 462–462. doi:10.1002/jrs.1318.
- [16] H. Luo, X. Zhou, C. Ellingford, Y. Zhang, S. Chen, K. Zhou, D. Zhang, C.R. Bowen, C. Wan, Interface design for high energy density polymer nanocomposites, *Chem. Soc. Rev.* 48 (2019) 4424–4465. doi:10.1039/C9CS00043G.
- [17] J. Tauc, R. Grigorovici, A. Vancu, Optical Properties and Electronic Structure of Amorphous Germanium, *Phys. Status Solidi.* 15 (1966) 627–637. doi:10.1002/pssb.19660150224.
- [18] J. Robertson, E.P. O'Reilly, Electronic and atomic structure of amorphous carbon, *Phys. Rev. B.* 35 (1987) 2946–2957. doi:10.1103/PhysRevB.35.2946.
- [19] D. Fink, W.H. Chung, R. Klett, A. Schmoltdt, J. Cardoso, R. Montiel, M.H. Vazquez, L. Wang, F. Hosoi, H. Omichi, P. Goppelt-Langer, Carbonaceous clusters in irradiated polymers as revealed by UV-Vis spectrometry, *Radiat. Eff. Defects Solids.* 133 (1995) 193–208. doi:10.1080/10420159508223990.
- [20] F. Kremer, A. Schönhal, *Broadband Dielectric Spectroscopy*, Springer Berlin Heidelberg, Berlin, Heidelberg, 2003. doi:10.1007/978-3-642-56120-7.
- [21] A. Alegria, J. Colmenero, Dielectric relaxation of polymers: segmental dynamics under structural constraints, *Soft Matter.* 12 (2016) 7709–7725. doi:10.1039/C6SM01298A.
- [22] P. Ben Ishai, M.S. Talary, A. Caduff, E. Levy, Y. Feldman, Electrode polarization in dielectric measurements: a review, *Meas. Sci. Technol.* 24 (2013) 102001. doi:10.1088/0957-0233/24/10/102001.
- [23] B. Wang, W. Huang, L. Chi, M. Al-Hashimi, T.J. Marks, A. Facchetti, High- k Gate Dielectrics for Emerging Flexible and Stretchable Electronics, *Chem. Rev.* 118 (2018) 5690–5754. doi:10.1021/acs.chemrev.8b00045.
- [24] K.C. Kao, Electric Polarization and Relaxation, *Dielectr. Phenom. Solids.* (2004) 41–114. doi:10.1016/b978-0-12-802903-9.00002-3.
- [25] J.W. Schultz, Dielectric Spectroscopy in Analysis of Polymers, in: *Encycl. Anal. Chem.*, John Wiley & Sons, Ltd, Chichester, UK, 2000: pp. 1–19. doi:10.1002/9780470027318.a2004.
- [26] M.-R. Tofighi, Interaction between electromagnetic waves and biological materials, in: *Princ. Appl. RF/Microwave Healthc. Biosensing*, Elsevier, 2017: pp. 53–101. doi:10.1016/B978-0-12-802903-9.00002-3.
- [27] G. Williams, D.C. Watts, Non-symmetrical dielectric relaxation behaviour arising from a simple empirical decay function, *Trans. Faraday Soc.* 66 (1970) 80. doi:10.1039/tf9706600080.
- [28] R. Bergman, General susceptibility functions for relaxations in disordered systems, *J.*

- Appl. Phys. 88 (2000) 1356–1365. doi:10.1063/1.373824.
- [29] A.K. Jonscher, Universal relaxation law: a sequel to Dielectric relaxation in solids, Chelsea Dielectrics Press, 1996.
- [30] J. Rydz, A. Šišková, A. Andicsová Eckstein, Scanning Electron Microscopy and Atomic Force Microscopy: Topographic and Dynamical Surface Studies of Blends, Composites, and Hybrid Functional Materials for Sustainable Future, *Adv. Mater. Sci. Eng.* 2019 (2019) 1–16. doi:10.1155/2019/6871785.
- [31] A. Ul-Hamid, *A Beginners' Guide to Scanning Electron Microscopy*, Springer International Publishing, Cham, 2018. doi:10.1007/978-3-319-98482-7.
- [32] C. Davisson, L.H. Germer, Diffraction of Electrons by a Crystal of Nickel, *Phys. Rev.* 30 (1927) 705–740. doi:10.1103/PhysRev.30.705.
- [33] L.C. Sawyer, D.T. Grubb, G.F. Meyers, *Polymer Microscopy*, Springer New York, New York, NY, 2008. doi:10.1007/978-0-387-72628-1.
- [34] R.F. Egerton, *Physical Principles of Electron Microscopy*, Springer International Publishing, Cham, 2016. doi:10.1007/978-3-319-39877-8.
- [35] B. Voigtländer, *Atomic Force Microscopy*, Springer International Publishing, Cham, 2019. doi:10.1007/978-3-030-13654-3.
- [36] A. Tripathi, A. Kumar, F. Singh, D. Kabiraj, D.K. Avasthi, J.C. Pivin, Ion irradiation induced surface modification studies of polymers using SPM, *Nucl. Instruments Methods Phys. Res. Sect. B Beam Interact. with Mater. Atoms.* 236 (2005) 186–194. doi:10.1016/j.nimb.2005.04.059.
- [37] D. Singh, N.L. Singh, A. Qureshi, P. Kulriya, A. Tripathi, D.K. Avasthi, A.N. Gulluoglu, Radiation induced modification of dielectric and structural properties of Cu/PMMA polymer composites, *J. Non. Cryst. Solids.* 356 (2010) 856–863. doi:10.1016/j.jnoncrysol.2010.01.006.
- [38] S. Shah, N.L. Singh, A. Qureshi, D. Singh, K.P. Singh, V. Shrinet, A. Tripathi, Dielectric and structural modification of proton beam irradiated polymer composite, *Nucl. Instruments Methods Phys. Res. Sect. B Beam Interact. with Mater. Atoms.* 266 (2008) 1768–1774. doi:10.1016/j.nimb.2007.11.061.